Journal of Materials Chemistry C

Accepted Manuscript

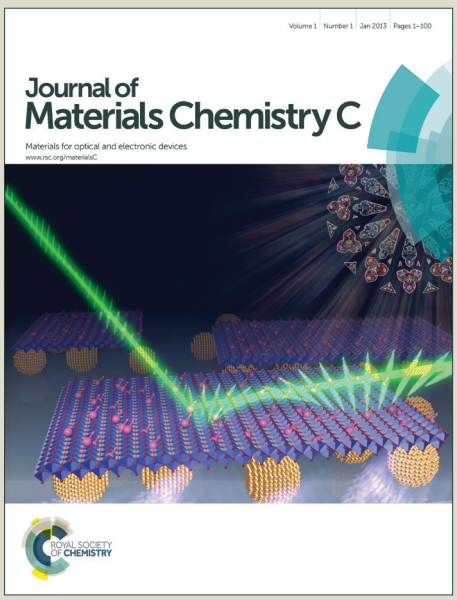

ROYAL SOCIETY OF CHEMISTRY

www.rsc.org/materialsC

Journal Name

ARTICLE

Thermoelectric transport and microstructure of optimized $Mg_2Si_{0.8}Sn_{0.2}$

Received 00th January 20xx,
Accepted 00th January 20xx

DOI: 10.1039/x0xx00000x

www.rsc.org/

J. de Boor,[a,+] S. Gupta,[a,+] H. Kolb,[a] T. Dasgupta,[b] and E. Müller[a,c]

Solid solutions from magnesium silicide and magnesium stannide exhibit excellent thermoelectric properties due to a favorable electronic band structure and a reduced thermal conductivity compared to the binary compounds. We have optimized the composition $Mg_2Si_{0.8}Sn_{0.2}$ by Sb doping and obtained a thermoelectric figure of merit close to unity. The material comprises of several phases and exhibits intrinsic nanostructuring. Nevertheless, the main features of the electronic transport can be understood within the framework of a single parabolic band model. Compared to Mg_2Si we observe a comparable power factor, a drastically reduced thermal conductivity and an increased effective mass.

Introduction

Thermoelectric materials can be used to convert (waste) heat directly into electrical energy. They can thus power autonomous devices or enhance the energy efficiency of various applications [1]. A relatively new approach is the use of thermoelectric materials as thermopower wave based energy sources. Such devices from nanoscale thermoelectric materials and chemical fuels employ high energy charge carriers in a non-equilibrium state to create considerable voltages and electrical power and may find application as miniature power source [2, 3]. The efficiency of the heat to electrical energy conversion is linked to the thermoelectric figure of merit of the materials, given by $ZT = \frac{\sigma S^2}{\kappa} T$. Here σ is the electrical conductivity, κ the thermal conductivity, S the Seebeck coefficient, and T the absolute temperature. Mg_2Si based solid solutions are among the most promising thermoelectric materials. For this material class a very desirable $ZT > 1$ has repeatedly been reported [4-9] and the constituting elements are abundant and non-toxic. Mg_2Si based solid solutions are therefore an efficient and environmentally compatible alternative to PbTe and skutterudites. Due to their very low density they are especially attractive for airborne or mobile applications where weight is crucial.

So far, most of the research is dedicated either to pure Mg_2Si due to its simplicity and the relatively high thermal stability or to Sn-rich compositions similar to $Mg_2Si_{0.4}Sn_{0.6}$. The latter composition exhibits a crossing of the Si and Sn sub-bands which increases the band degeneracy and therefore drastically increases the effective mass of the electrons [4, 5, 10]. Furthermore the thermal conductivity is reduced compared to the binary compositions due to additional alloy scattering. There are only a few reports on the Si-rich side of the $Mg_2(Si,Sn)$ family. Tani *et al.* optimized carrier concentration for $Mg_2Si_{1-x}Sn_x$ for x=0.05 and 0.1, reaching a ZT_{max} of 0.68 at 864 K [11]. Liu *et al.* and Samunin *et al.* reported some transport data for $x = 0.2$ and showed a maximum ZT of around 0.8 but did not present a conclusive optimization with respect to carrier concentration [5, 12].

However, investigation and optimization of Si-rich $Mg_2(Si,Sn)$, in particular $Mg_2Si_{0.8}Sn_{0.2}$, is very interesting both from a fundamental and an applied point of view. $Mg_2Si_{0.8}Sn_{0.2}$ has a significantly lower density than $Mg_2Si_{0.4}Sn_{0.6}$ ($2.3\ gcm^{-3} < 3\ gcm^{-3}$), i.e. for applications where weight is a crucial factor it might be the optimal choice, even with inferior thermoelectric performance. Moreover, as Mg_2Si is thermally and chemically more stable than Mg_2Sn it is plausible that Si-rich compositions are more stable than Sn-rich compositions, allowing operation at higher temperatures. Furthermore, $Mg_2Si_{0.8}Sn_{0.2}$ is closer to the technologically more developed Mg_2Si, where progress in contact development has been reported [13, 14]. On the other hand, compared to Mg_2Si an improvement of the thermoelectric properties can be expected due to increased phonon alloy scattering.

Beyond that, the composition $Mg_2Si_{0.8}Sn_{0.2}$ is also very interesting with respect to fundamental aspects. According to literature reports there is a miscibility gap between Mg_2Si and Mg_2Sn whose exact borders are disputed [4, 15-17]. According to Ref. [16] $Mg_2Si_{0.8}Sn_{0.2}$ is within the miscibility gap. This provides the chance for an intrinsic nanostructure within the material, decreasing the thermal conductivity and thus enhancing the thermoelectric performance. This strategy has successfully been employed e.g. for the PbTe family and Half-Heuslers [18, 19].

[a] Institute of Materials Research, German Aerospace Center, Linder Höhe, 51147 Köln, Germany
[b] Dept. of Metallurgical Engineering and Materials Science, Indian Institute of Technology Bombay, Mumbai 400076, India
[c] Institute for Inorganic and Analytical Chemistry, Justus-Liebig-Universität Gießen, Heinrich-Buff-Ring 58, 35392 Gießen, Germany
† contributed equally.

Electronic Supplementary Information (ESI) available: [details of any supplementary information available should be included here]. See DOI: 10.1039/x0xx00000x

Modeling of the $Mg_2(Si,Sn)$ family is important for thorough understanding and further optimization. This modeling is often performed using a linear interpolation between Mg_2Si and Mg_2Sn for parameters like band gaps or interaction potentials [4, 20, 21]. These theoretical assumptions have to be validated by experimental results.

In this work we have therefore studied the microstructure and the thermoelectric properties of $Mg_2Si_{0.8}Sn_{0.2}$. We demonstrate charge carrier density optimization by means of Sb doping. High temperature measurements of electrical and thermal conductivity, Seebeck coefficient as well as Hall carrier density and mobility reveal that the electronic properties can be modelled reasonably well in the framework of a single parabolic band model. The experimental and the modeling results provide fundamental transport parameters like effective mass, carrier mobility and interaction potentials. Additionally we compare our results with data from the binary compound Mg_2Si and provide inside into the effect of Si/Sn substitution on the electronic band structure.

Experimental

$Mg_2Si_{0.8-y}Sn_{0.2}Sb_y$ ingot material was synthesized by direct melting of the elements in an induction furnace as described in [22]. Sb is a well-known n-type dopant for $Mg_2(Si,Sn)$ and was added to tune the carrier concentration. To compensate for the loss of Mg due to evaporation during the melting process 5% excess were added. The ingot material was crushed in air using agate mortar and pestle. Pellets with a diameter of $15\ \mathrm{mm}$ and a height of roughly $1\ \mathrm{mm}$ were obtained by compaction at 850°C using current assisted sintering. Further sintering details can e.g. be found in [23]. Electrical conductivity σ and Seebeck coefficient S of the samples were measured concurrently using a custom-built setup. Setup and details on the data analysis can be found elsewhere [24, 25]. The thermal conductivity κ of the samples was determined from $\kappa = D\rho c_p$, where the thermal diffusivity D was measured using a commercial LFA-setup (Netzsch) and the density ρ using Archimedes` method. The Dulong-Petit value was used for specific heat c_p calculation. Hall carrier concentration n_H and mobility μ_H were determined in a van der Pauw geometry using a custom-built setup with a variable magnetic field [26, 27]. XRD data was obtained using a Siemens D5000 and Rietveld refinement of the lattice parameter a was performed using Topas 4.2. SEM images were taken using a Zeiss Ultra 55 equipped with an EDX detector. Measurement uncertainties are 5% for σ and S, 8% for κ and 15% for carrier concentration and mobility. This results in a total uncertainty of 12% for the thermoelectric figure of merit if we sum the errors squared and assume that they are independent of each other and 23% as worst case scenario. Note also that here the total measurement uncertainty is given, whereas the reproducibility is usually better by a factor of two.

Results

Table 1 shows the nominal composition of five synthesized samples as well as the measured densities ρ. Densities have been obtained using sample geometry and weight as well as employing Archimedes' principle. Comparing both methods the geometrical density ρ_{geo} has the higher uncertainty; however the Archimedes density ρ_A tends to overestimate the density in principle as it does not account for open porosity in the material. The results for both densities are similar within the experimental errors, except for sample #3. This indicates that there is little open porosity in the samples. The density can be used to estimate the Sn content x of the samples: $x \approx \frac{\rho - \rho_{Mg2Si}}{\rho_{Mg2Sn} - \rho_{Mg2Si}}$. We used the Archimedes density for this calculation as the geometrical density is prone to underestimate the Sn content in case of open porosity in the samples. The thus calculated Sn content is smaller than the nominal content of $x = 0.2$ but shows some increase with increasing Sb concentration.

Table 1: Sample properties: nominal composition, densities, and Sn content x calculated from density and XRD data.

Nominal composition		ρ_{geo} [g/cm³]	ρ_A [g/cm³]	x from ρ_A	x from XRD
$Mg_2Si_{0.8}Sn_{0.2}$	#1	2.17	2.21	0.132	0.128
$Mg_2Si_{0.795}Sn_{0.2}Sb_{0.005}$	#2	2.25	2.24	0.145	0.140
$Mg_2Si_{0.79}Sn_{0.2}Sb_{0.01}$	#3	2.12	2.21	0.128	0.117
$Mg_2Si_{0.785}Sn_{0.2}Sb_{0.015}$	#4	2.33	2.31	0.174	0.170
$Mg_2Si_{0.78}Sn_{0.2}Sb_{0.02}$	#5	2.29	2.31	0.168	0.170

Figure 1 shows the XRD results. All mayor peaks can be indexed according to the reported anti-fluorite structure (space group *Fm-3m*) of Mg_2Si and Mg_2Sn. The minor peak at $2\theta \approx 43°$ corresponds to MgO, an impurity often observed in this material class [28].The zoom in around the 220 peak in Figure 1b) shows that the peaks are relatively broad and show a shift towards smaller angles, i.e. larger lattice constant compared to Mg_2Si.

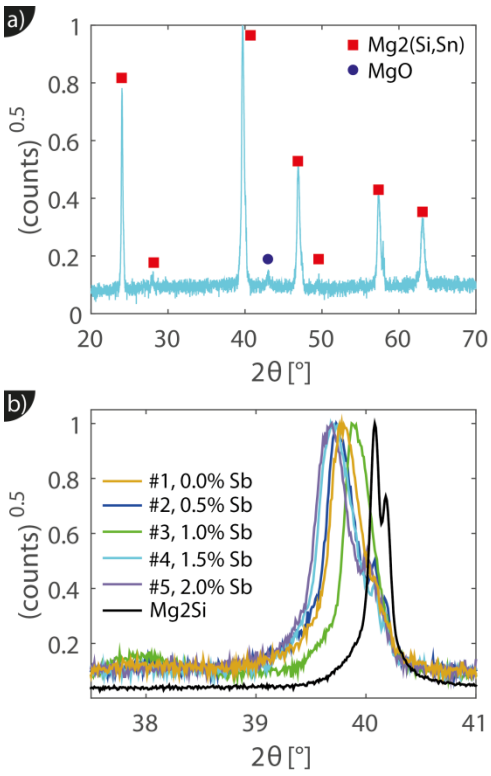

Figure 1: a) X-ray diffraction data of sample #2.All mayor peaks can be indexed as (shifted) Mg_2Si peaks. Minor peaks for MgO can also be observed. b) The zoom-in around the (220) peak reveals peak broadening and emphasizes the shift compared to an Mg_2Si sample.

The relation between lattice constant a and Sn content x is approximately given by $x = (a - a_{Mg2Si})/(0.0427\ nm)$ [20]. The calculated values for x are given in Table 1 and confirm the results and trends from the density data. In fact the good agreement between the Sn content from density and XRD peak shift indicates good compaction and a high relative density of the samples, as significant (closed) porosity would lead to a reduced x from the density data but would not affect that from the XRD peak shift.

Microstructural analysis by SEM shows a multiphase sample with a matrix in grey and minor phases in light grey and dark grey, see Figure 2. The image is taken from the sample #5, but the microstructure is similar in all samples, see supporting Figures S2-S4. EDX analysis of all samples reveals that the matrix and the minor phases itself do not have a sharp composition, but consist of domains with similar, yet distinct local compositions.

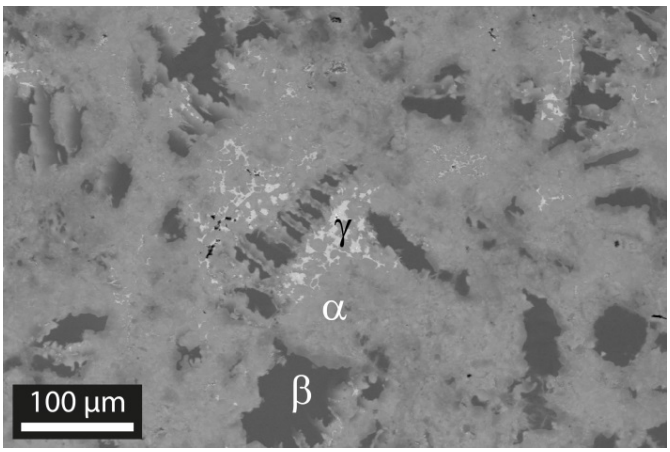

Figure 2: Backscattered image of sample #5. Three different phases are clearly distinguishable: the main phase $\boldsymbol{\alpha}$, the Mg_2Si-like phase $\boldsymbol{\beta}$ and a Sn-rich phase $\boldsymbol{\gamma}$. EDX analysis reveals that these phases itself show significant local concentration fluctuations.

The Sn content x as well as the approximate phase fractions are given in Table 2. Employing the distinct grey values of the three phases the graphical analysis software ImageJ has been used to estimate the (areal) fraction each phase. It yields 85% main phase, 13% of the Mg_2Si-like phase and about 2% for the Sn-rich phase for the two-dimensional image. To calculate the 3D values we assumed that the main phase is the matrix and the minor phases are isotropically included within the matrix. The phase fraction for the minor phases is then given by $z_{2D}^{3/2}$, where z_{2D} is the fraction in the two dimensional image.

Table 2: Sn content x and phase fraction of a typical $Mg_2Si_{0.8}Sn_{0.2}$ sample.

	Main phase	Si-rich phase (dark)	Sn-rich phase (bright)
Sn content x	$0.1 < x < 0.2$	$x < 0.03$	$0.4 < x < 0.6$
Phase fraction	0.95	0.05	<0.01

Figure 3 shows an element mapping of a typical $Mg_2Si_{0.8}Sn_{0.2}$ sample. The Mg_2Si-like and the main phase are clearly distinguishable, and it can also be seen that the matrix phase itself has a spatially varying Sn content. Another interesting feature is the observed difference in Sb content for main phase and Mg_2Si-like phase. Sb is significantly more dissolved in the main phase with the higher Sn content. Presumably Sb can be more easily incorporated in Sn-richer phases due to their larger lattice constant. The EDX analysis also detects some oxygen, mainly at interface regions between the matrix phase and the Mg_2Si-like phase. As MgO has been identified by XRD it can be deduced that oxygen is present presumably in form of MgO. The matrix phase and the Mg_2Si like phase are also visible in the Mg mapping. As the lattice constant increases with increasing Sn content the Mg density is higher in the Mg_2Si-like phase than in the matrix phase which results in the observed contrast.

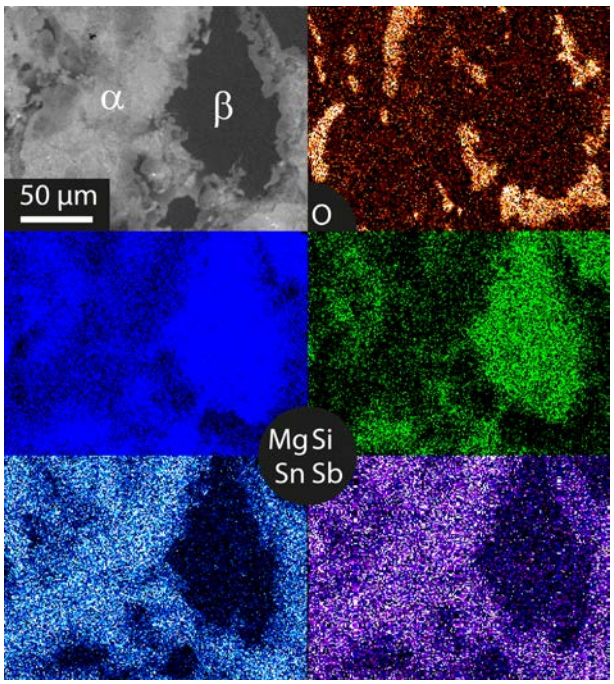

Figure 3: BSE image and elemental mapping for O, Mg, Si, Sn and Sb.

Transport data

Despite the microstructure the samples exhibit a good macroscopic homogeneity of their electronic properties as evidenced by a local mapping of the Seebeck coefficient (see supporting Figure S6).

Transport data for $Mg_2Si_{0.8-y}Sn_{0.2}Sb_y$ is shown from room temperature to 740 K in Figure 4. Due to better visibility only the thermal conductivity data of the undoped sample (#1) is shown here, the complete data is presented in Figure S5 of the supporting material. The electrical conductivity (a) shows the typical decrease with increasing temperature of a highly doped semiconductor above 400 K; below 400 K a plateau can be observed for some of the samples. The electrical conductivity also exhibits the expected increase with increasing doping. The Seebeck coefficient (b) decreases with increasing doping and increases approximately linear with increasing temperature for all samples.

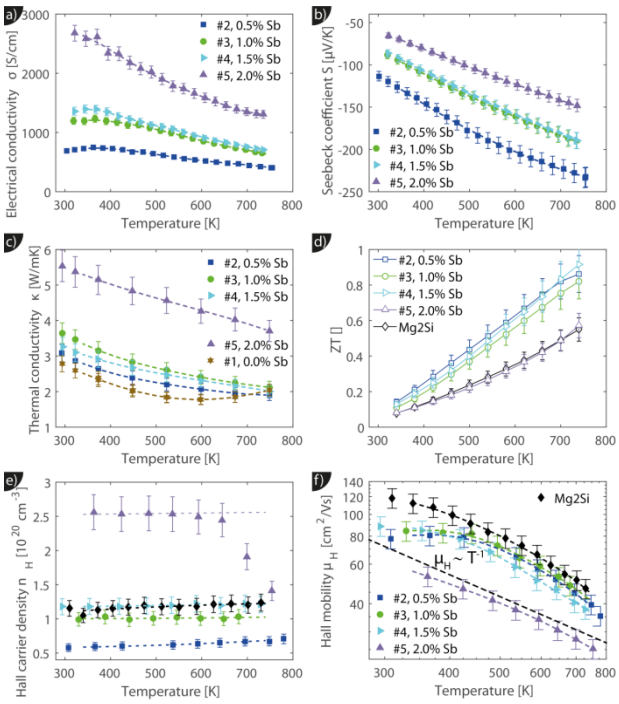

Figure 4: Transport measurement data for $Mg_2Si_{0.8-y}Sn_{0.2}Sb_y$ samples. Full markers indicate measurement data, empty markers calculated data and the dashed lines indicate the fitted transport data that is used for modeling. The thermoelectric figure of merit (d) as well as Hall carrier concentration and mobility are also presented for a sample with composition $Mg_2Si_{0.9875}Sb_{0.0125}$ (i.e. without tin) for comparison. This sample is labelled as "Mg2Si".

The thermal conductivity (c) decreases with temperature for all samples but shows a much higher value for the sample with highest doping. The thermoelectric figure of merit ZT is calculated from a)-c) and shows an increase with temperature for all samples. Sample #4 with $y = 0.015$ has the highest thermoelectric figure of merit with $ZT = 0.95$ at 740 K. While the ZT values for the less doped samples are lower but comparable, sample #5 has a drastically lower figure of merit. Figure 4e) reveals a roughly temperature independent carrier density for all samples, except for sample #5. Here the carrier concentration is roughly constant up to 650 K after which n_H decreases rapidly. As the sample has been stable during the $S - \sigma$ and the LFA measurement beforehand we don't know what caused the irreversible change in the sample. It can be seen that the carrier density data for the samples is consistent with the results for S and σ and that the control over carrier concentration is not perfect as the actual Hall carrier concentration does not exactly follow the linear trend expected from the nominal doping composition. The doping is relatively effective as one would roughly expect $1.5\ 10^{20} cm^{-3}$ carriers for a nominal composition of $Mg_2Si_{0.79}Sn_{0.2}Sb_{0.01}$ if one carrier per Sb atom is provided. The Hall mobility (f) decreases with increasing temperature after an initial plateau for sample #2-#4; sample #5 shows a monotonic trend with significantly lower absolute values.

We now want to analyze the results in the frame work of a single parabolic band model (SPB) [29]. This model has been employed for Mg_2Si and $Mg_2Si_{1-x}Sn_x$ with reasonable success

beforehand [5, 21, 30]. For $T > 500$ K holds $\mu_H \propto T^{-p}$ with $1 < p < 1.5$, which indicates acoustic phonon (AP) scattering as dominant scattering mechanism. For lower temperatures there is some deviation from this behavior, presumably due to grain boundary scattering of the charge carriers at the interfaces [28]. A possible influence of alloy scattering can not be excluded but is not expected to be dominant due to the relatively low Sn content [6]. Grain boundary scattering is an extrinsic scattering mechanism so that AP scattering can assumed to be the dominant intrinsic mechanism at all temperatures. In this case the reduced chemical potential η and the DOS effective mass m^* of the electrons can be calculated using

$$S = -\frac{k}{e}\left(\frac{2F_1(\eta)}{F_0(\eta)} - \eta\right), \quad (1)$$

and

$$n = 4\pi\left(\frac{2m^* k_B T}{h^2}\right)^{3/2} F_{1/2}(\eta). \quad (2)$$

Here e is the elementary charge, k_B Boltzmann's constant, F_i the Fermi integral of order i, and the reduced chemical potential η is given by $\eta = \frac{E_F}{k_B T}$. The measured Hall carrier density n_H is linked to the true carrier density by $n_H = n/r_H$ with the Hall scattering factor given by $r_H = \frac{1.5F_{0.5}F_{-0.5}}{2F_0^2}$. The chemical potential for sample #2-#5 is plotted in Figure 5a). It can be seen that the chemical potential lies above the conduction band edge at room temperature for all samples. It decreases with increasing temperature and crosses the band edge for the lowest doped sample.

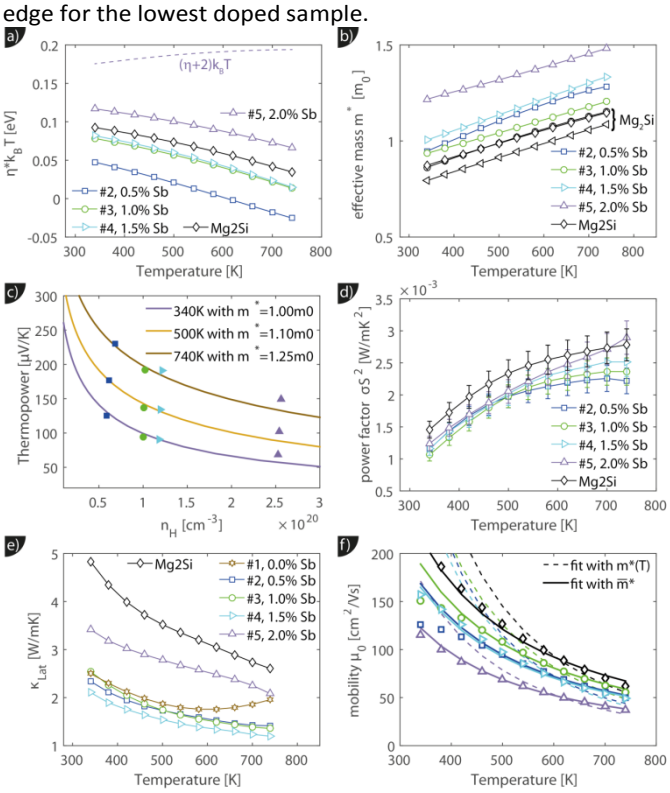

Figure 5: Results from the single parabolic band model for $Mg_2Si_{0.8-y}Sn_{0.2}Sb_y$; for comparison also the data of $Mg_2Si_{0.9875}Sb_{0.0125}$ ("Mg2Si") from [28] are presented. a) shows the calculated chemical potential for all samples. For the sample with the largest carrier concentration (#5) $(\eta + 2)k_B T$ is plotted as well, this gives an impression up to which energy a significant number of carriers are excited. b) all samples show an increase in effective mass with increasing temperature, with the sample #5 having a significantly higher effective mass. c) The Pisarenko-plot shows decent agreement between experimental data and theoretical curves using the temperature dependent effective masses of b). d,e) Power factor σS^2 and lattice thermal conductivity (overlaid by bipolar contribution). Compared to Mg_2Si the $Mg_2Si_{0.8}Sn_{0.2}$ samples show a slightly reduced power factor but a drastically reduced lattice thermal conductivity. f) A fit of the mobility parameter μ_0 vs T can be used to obtain the deformation potential. Dashed lines show the result using $m^*(T)$ while the solid lines result from an averaged effective mass.

The effective mass increases with temperature for all samples. While the three lower doped samples increase roughly from $1\,m_0$ to $1.25\,m_0$ in the measured temperature range, the sample with the highest doping increases from $1.25\,m_0$ to $1.35\,m_0$; m_0 is the free electron mass. The Pisarenko plot in Figure 5c) shows reasonable agreement between the experimental and the modeling data.

The lattice thermal conductivity (plus the bipolar contribution) is plotted in Figure 5e). It is given by $\kappa_{lat} + \kappa_{bip} = \kappa - L\sigma T$, with $L = \frac{k^2}{e^2}\frac{3F_0F_2 - 4F_1^2}{F_0^2}$ for the SPB model with AP scattering. The thermal conductivities of sample #1-#4 are comparable with a slight reduction for increasing doping. The lattice thermal conductivity follows a power law $\kappa_{lat} = A + B/T^p$ with $-1 < p < -0.5$. Umklapp phonon scattering predicts a $\kappa_{lat} \propto T^{-1}$ behavior, while $\kappa_{lat} \propto T^{-0.5}$ corresponds to alloy scattering as dominant phonon scattering mechanism. The measurement results therefore indicate a mixed scattering mechanism. At high temperature the onset of the bipolar contribution is clearly visible for the undoped sample. The sample with the highest doping has a lattice thermal conductivity which is more than 50% higher than the others, indicating significantly different thermal transport in this sample.

The carrier density independent mobility μ_0 is plotted in Figure 5f) and is connected to the Hall mobility by $\mu_{H,AP} = \frac{F_{-0.5}}{2F_0} * \mu_0$ [29]. It is a material parameter and thus supposed to be independent of carrier concentration. Indeed one notices that the mobilities for sample #2-#4 are very similar. The mobility of sample #5 is significantly lower; however, the difference is not as large as for μ_H. The mobility data can be used to extract a further material parameter, the deformation potential E_{Def} which quantifies the interaction between acoustic phonons and charge carriers. It is given by [31]

$$\mu_0 = \frac{e\pi\hbar^4}{\sqrt{2}(kT)^{1.5}}\frac{1}{(m_i)^{2.5}} * \frac{C_{11}}{E_{\mathrm{def}}^2} = A(T) * \frac{C_{11}}{E_{\mathrm{def}}^2} * \frac{1}{T^{1.5}}. \quad (3)$$

Figure 5f) shows fits of Eq. (3) to the experimental data using the $m^*(T)$ as shown in Figure 5b) (dashed lines) and an average effective mass that is constant with temperature (full lines).

The thermoelectric potential of the material can be estimated by calculating $ZT(n,T)$. The basic equation can be rearranged to

$$ZT = \frac{S^2}{L + (\psi\beta)^{-1}} \quad (4)$$

with $\psi = \frac{8\pi e}{3}\left(\frac{2mk_b}{h^2}\right)^{1.5} F_0$, $\beta = \mu_0 \left(\frac{m^*}{m}\right)^{1.5} T^{2.5}/\kappa_l$, and $\mu_0 = \mu_H * 2F_0/F_{-0.5}$. The material parameter β is plotted in Figure S7d). For the theoretical curves shown in Figure 6 the average β of sample #2-#4 has been employed.

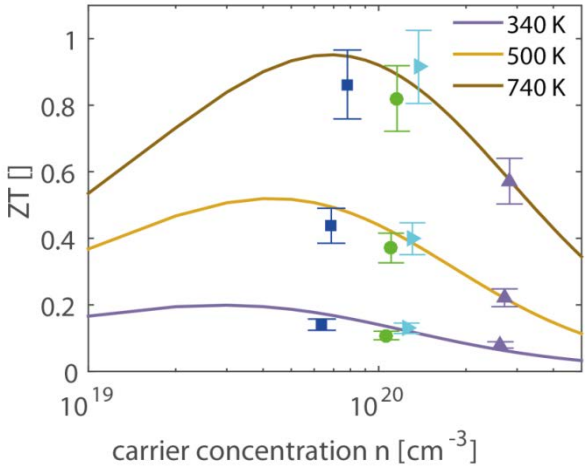

Figure 6: Experimental and theoretical results of the thermoelectric figure of merit vs carrier concentration at different temperatures.

The results from Eq. (4) show the expected trends: an increase for ZT_{max} with increasing temperature and a shift of the optimal carrier concentration towards higher values for increasing temperature. Our experimental data shows good agreement with the modeling results. ZT_{max} both from the SPB model and the experimental data is ≈ 0.95 at 740 K. The best experimental value is at $n_{opt} = 1.2 * 10^{20}\ cm^{-3}$, while the model predicts $0.7 * 10^{20}\ cm^{-3}$; however, the maximum is relatively broad and the model does not account for differences in κ_{lat} observed between the samples.

Discussion

Microstructure

XRD and density measurements confirm the successful synthesis of $Mg_2Si_{1-x-y}Sn_xSb_y$ with $x \approx 0.15$. This is slightly smaller than can be expected from the initial weight stoichiometry. We suspect that some elemental Sn is lost during the synthesis process. Sn content values from XRD peak shift as well as from Archimedes density compare well with each other and show the same minor increase of x with increasing dopant concentration. It is well known from other material classes (e.g. $CoSb_3$ type skutterudites [32]) that small changes in the composition can influence the solubility of one of the components in the material. This is plausible in this case because the targeted composition is close to the edge of the reported miscibility gap. The electron microscope investigations reveal multiphase samples composed out of three different phases. However, these phases are not homogeneous but consist of domains with similar but distinct stoichiometry. The main phase has a Sn content of $0.1 < x < 0.2$ and comprises around 95% of the material volume. The second phase with 5%vol is Mg_2Si-like with $x < 0.03$. The third phase has $< 1\%$vol and $0.4 < x < 0.6$. These observations are in agreement with the reported miscibility gap between Mg_2Si and Mg_2Sn. Our results are also in quantitative agreement with the data from [16] taking into account that EDX analysis will give a lower limit for x at the left side of the miscibility gap and an upper limit for the right side due to the limited spatial resolution.

Our SEM/EDX results confirm the XRD results where the observed broad peaks indicate stoichiometric variations. The observed minor phases can very well be hidden in the shoulders of the broad peaks. EDX mapping also shows a lower content of the dopant Sb in the Mg_2Si-like phase compared to the matrix phase. As the matrix phase will have a slightly larger lattice constant a better Sb solubility can be expected.

Transport data

We have obtained ZT_{Max} =0.95 at 740 K, higher than previous reports on the same composition. Liu *et al.* and Samunin *et al.* both obtained a ZT_{max} around 0.8 [5, 12]. The samples investigated by Liu *et al.* exhibit a slightly higher power factor than our samples but a significantly higher thermal conductivity. Tani *et al.* studied the composition $Mg_2Si_{0.9}Sn_{0.1}$ and obtained $ZT_{max} = 0.68$ at 864 K. Comparing our transport data with the work of Tani *et al.* on $Mg_2Si_{0.9}Sn_{0.1}$ we find similar power factors but a higher lattice thermal conductivity in their work [11]. A possible explanation is the intrinsic nanostructuring in our samples due to the existence of three distinct phases as well as the compositional variations within these phases. This characteristic has not been discussed in the previous reports; however, as no details on microstructure are given in these papers a thorough comparison is difficult. We also note that our lattice thermal conductivity for sample #1-#4 are in good agreement with the experimental and theoretical result at room temperature from Zaitsev *et al.* [33]. The significantly higher thermal conductivity of #5 has to be related to the microstructure of the sample, however, since microstructural investigations have not revealed a fundamental difference between #5 and #2-#4, further investigations are required.

Electronic transport analysis

We have modeled the electronic transport properties within the SPB model with AP scattering as dominant scattering mechanism. Overall the agreement of experimental data and modeling predictions is good. At low temperatures the fingerprint of a second scattering mechanism is visible in σ which can be related to the observed MgO in the samples. It has been shown that MgO can cause additional grain boundary scattering and hence reduce carrier mobility and electrical conductivity. [28, 34]. The main parameters used in or extracted from the model are summarized in Table 3.

Table 3: SPB parameters. For m^* and κ_{lat} the average value from samples #2-#4 is given.

T	n_{opt} [10^{19} cm^{-3}]	ZT_{max}	m^* [m_0]	κ_{lat} [W/ mK]	E_{Def} [eV]
340	3	0.2	1	2.3	13.0
740	7	0.95	1.25	1.3	13.0

We find an optimum carrier concentration n_{opt} which is lower than the value ($n_{opt} = 18 * 10^{19}\ cm^{-3}$) stated by Liu *et al.* [5], however the carrier concentration optimization was mainly performed in view of compositions with higher Sn content in their work. With respect to the effective mass we find good agreement with literature: Liu et al obtained $m^* = 0.93\ m_0$ for $Mg_2Si_{0.8}Sn_{0.2}$ while Tani *et al.* obtained $m^* = 0.9\ m_0$ for $Mg_2Si_{0.9}Sn_{0.1}$ at room temperature.

However, there are also deviations from the SPB model. Firstly, we observe an apparent increase of the carrier concentration (see Figure 4 for $n_H(T)$ or Figure S7b) for $n(T)$). Secondly, we find a clear increase in effective mass with temperature and a difference between the sample with the highest doping (#5) and the other samples. Thirdly, the carrier density corrected mobility μ_0 differs for sample #5 compared to samples #2-#4 (see Figure 5f)), although it is a material parameter and supposed to be independent of carrier concentrations.

The increase in n and m^* with T was similarly found in Mg_2Si [28, 30] and might be due to the non-parabolicity of the bands. The observed difference in m^* for #5 compared to #2-#4 could either be due to a non-parabolic band or by the influence of the second conduction band with higher m^*: $Mg_2Si_{1-x}Sn_x$ has two threefold degenerate conduction bands CB_L and CB_H with a band gap E_0 that depends on x. For small x the light conduction band is at a lower energy, while at large x the heavy band is at lower energy. The cross-over is around $= 0.6$ [5, 10]. Less clear is the band gap between the two conduction bands for arbitrary x. Zaitsev *et al.* used $E_{0,x=0} = 0.4\ eV$ (with CB_L closer to the valence band) and $E_{0,x=1} = 0.2\ eV$ (with CB_H closer to the valence band). They suggested a linear interpolation in between which would result in $E_{0,x=0.2} = 0.28\ eV$ [4]. Bahk *et al.* used the same assumption for a recent transport modeling [20]. On the other hand, Bourgeois *et al.* calculated $E_{0,x=0} = 0.19\ eV$ and $E_{0,x=1} = 0.28\ eV$ which would correspond to $E_{0,x=0.2} = 0.1\ eV$, i.e. a much smaller band gap for the investigated composition [15]. Tan *et al.* calculated the interband gaps using DFT for different composition obtaining $E_{0,x=0.25} \approx 0.3\ eV$ [35]. The discrepancy in the literature shows that the interband gap is not well characterized, the less as the band positions are temperature dependent and the calculations do not account for this.

One possible explanation for the experimentally observed increase in m^* for sample #5 compared to #2-#4 is thus a contribution of the second conduction band CB_H to the electronic transport. If CB_H is within $(\eta + 2)k_BT$ some contribution can be expected. Figure 5a) indicates that this would be the case for $E_0 \leq 0.2\ eV$. On the other hand DFT calculations have shown that the bands of $Mg_2(Si,Sn)$ are not strictly parabolic and therefore the effective mass itself depends on the chemical potential [35, 36]. In this case, however, the density-of-states effective mass, that is related to the band shape is not identical to the momentum effective mass (which controls the transport integrals) anymore[37]. Considering only the effective mass data can thus not provide clear evidence on E_0 and the question whether one or two bands contribute. Further insight can be gained by a detailed analysis of the mobility data.The fits of $\mu_0(T)$ to extract the electron acoustic phonon interaction parameter E_{Def} are plotted using $m^*(T)$ as shown in Figure 5f) as dashed lines. The fit is performed in the temperature region where AP scattering is clearly dominant, i.e. above 500 K. The agreement between experimental data and theoretical result is not very good, in particular with respect to the temperature dependence. As the strong temperature dependence of $m^*(T)$ is unexpected and might be an artifact of the assumed parabolic band structure we have also fitted the data using the average, temperature independent m^* of each sample. The result is plotted in full lines and is in almost perfect agreement with the experimental data above 450 K. This indicates that the observed apparent increase in $m^*(T)$ is indeed an artifact of the simple SPB model assumptions.

The phonon deformation potential can be extracted from the fit if the elastic constant C_{11} is known. As this is not the case for this particular composition we have used a linear interpolation of the experimental room temperature values from Mg_2Si and Mg_2Sn yielding $C_{11,\ x=0.2} \approx 110\ GPa$ [38, 39]. This is in decent agreement with preliminary data from resonant ultrasonic spectroscopy giving $\approx 100\ GPa$ [40]. The fitting results for E_{Def} of sample #2-#5 are $13.1\ eV, 13.5\ eV, 12.8\ eV, 12.8\ eV$, giving an average value of $E_{Def,x=0.2} = 13.0\ eV$. The good agreement between the results for each sample (although μ_0 is different) firstly increases the credibility of the result for $E_{Def,x=0.2}$ and secondly argues against a significant influence of a second band CB_H on the electronic transport: as the deformation potential for the two sub bands differs by more than 50% [6] one should see a difference for E_{Def} between #5 and samples #2-#4. This as well as the much better fits of $\mu_0(T)$ for a temperature-independent m^* indicate that the observed differences in the mobility parameter μ_0 between the samples and the apparent temperature dependent m^* are rather the consequences of a not strictly parabolic band CB_L than due to a second band contributing to the transport.

Our result for E_{Def} is higher than the value used by Bahk *et al.* $E_{Def,x=0.2} = 8.9\ eV$. The difference is not due to the mobility data but rather the used elastic constant. Bakh *et al.* used $C_{11,\ x=0.2} \approx 40\ GPa$, i.e. a much lower value. If we use the same elastic constant we obtain $E_{Def,x=0.2} \approx 7.9\ eV$ in good agreement with their data. This disagreement can be figured out by a mapping of the elastic constants with temperature and composition. Liu *et al.* obtained $E_{Def,\ x=0} = 17\ eV$ and

$E_{Def\ x=1} = 10\ eV$ which gives $E_{Def\ x=0.2} = 15.4\ eV$ in the linear interpolation; in decent agreement with our results [6].

Comparison with Mg_2Si

Further insight into fundamental trends can be gained by comparing the obtained material parameters of $Mg_2Si_{0.8}Sn_{0.2}$ with those of the parental compound Mg_2Si. We have therefore plotted the relevant transport data and modeling results of a sample with composition $Mg_2Si_{0.9875}Sb_{0.0125}$ in Figure 4 and Figure 5, labelled as "Mg2Si". Dopant concentration and compaction parameters were optimized giving $ZT > 0.7$ at 800 K, the sample might therefore serve as valid comparison [23, 28, 41]. Formation of a solid solution and the observed multiphase character of the $Mg_2Si_{0.8}Sn_{0.2}$ samples affect the power factor only to a small extend but reduce the lattice thermal conductivity by a factor of two over the whole measurement range. The general trends are not unexpected and have been observed previously [4, 5]. We furthermore observe a small reduction in charge carrier mobility which is partly due to additional alloy scattering at the Sn atoms [42] and partly due to the microstructure. The more fundamental question is if and how variations in stoichiometry influence the band structure. In the model employed by Zaitsev and others a change in the Si/Sn ratio results in a *shift* of conduction bands CB_L and CB_H with respect to each other (and the valence bands) but the *curvature* of the bands remains unaffected [4, 5, 20]. Our measurement results indicate differently as we find an increase in effective mass upon Sn substitution (see Figure 5b) indicating a flattening of the CB_L band. The increase in effective mass with increasing Sn content is in agreement with DFT results from Tan *et al.* [35]. We furthermore observe a slight reduction of the deformation potential. The mean value for $Mg_2Si_{0.8}Sn_{0.2}$ is $E_{Def,\ x=0.2} = 13.0\ eV$, while we found $E_{Def,\ x=0} = 15\ eV$ for the compound without Sn, see Figure 5f and Ref. [28].

Overall the main features of the electronic transport can be well understood in the framework of a single parabolic band although the material is not a single phase compound and has a complex microstructure. It is plausible that the matrix phase is dominant for the carrier transport as the Sn-rich phase has only a very small volume fraction (<1%) and the Mg_2Si-like phase is significantly less doped and therefore behaving more or less like insulating particles within the matrix. The dependence of $m^*(T, \eta)$ indicates that the bands are not strictly parabolic. Nevertheless, the agreement between experimental data and the predictions from the simple single parabolic band model is good and material parameters like $n_{opt}, ZT_{Max}, m^*, E_{Def}$ can expected to be reasonable accurate. The observed deviations from the single parabolic band model point towards a non-parabolic band, rather than a contribution from the second band. This indicates a band gap between the light and the heavy conduction band of $\geq 0.2\ eV$, supporting earlier work from Zaitsev *et al.* [4] and calculations from Liu *et al.* [5], but in contradiction to theoretical results from Bourgeois *et al.* [15]. However, an effect of the second band can not be totally excluded from the data. We also note that a Kane type band would lead to a lower Seebeck coefficient at high doping than a parabolic band, in contrast to what is found experimentally. More sophisticated modeling is therefore required for a full assessment of the band structure.

Comparing properties of $Mg_2Si_{0.8}Sn_{0.2}$ with those of Mg_2Si we reveal a reduction of the phonon deformation potential and an increase in effective mass, indicating a band flattening upon Sn substitution.

Conclusions

We have successfully synthesized $Mg_2Si_{0.8-y}Sn_{0.2}Sb_y$. The samples show a heterogeneous microstructure and multiphase character. The main phase itself does not have one strict composition but is composed of various domains with similar compositions. We determine a maximum thermoelectric figure of merit of 0.95 at 740 K, the best reported for this composition. The specific figure of merit is comparable to the results for $Mg_2Si_{0.4}Sn_{0.6}$; $Mg_2Si_{0.8}Sn_{0.2}$ might thus find an application where material weight is a crucial factor, i.e. in airborne applications. We furthermore show that the electronic transport can be modelled within a simple single parabolic model with reasonable accuracy. This allows for the extraction of fundamental material parameters like effective mass and the phonon deformation potential. Comparison with Mg_2Si shows a flattening of the light conduction band, indicating that substitution of Si by Sn does not only affect the band energies but also their curvature.

Acknowledgements

The authors would like to thank W. Schönau and P. Blaschkewitz for support with the thermoelectric measurements, and A. Francke and P. Watermeyer for their help with the electron microscope. Furthermore B. Klobes is acknowledged for useful discussion on elastic constants and K. Kelm for discussion on microstructure and phase diagrams. Special thanks to Jeff Snyder for insight on band structures and effective masses as well as to the Helmholtz Association for endorsement.

References

1. G. S. Snyder and E. S. Toberer, *Nat. Mater.*, 2008, **7**, 105-114.
2. W. Choi, S. Hong, J. T. Abrahamson, J. H. Han, C. Song, N. Nair, S. Baik and M. S. Strano, *Nat. Mater.*, 2010, **9**, 423-429.
3. S. Walia, S. Balendhran, P. Yi, D. Yao, S. Zhuiykov, M. Pannirselvam, R. Weber, M. S. Strano, M. Bhaskaran, S. Sriram and K. Kalantar-zadeh, *J Phys Chem C*, 2013, **117**, 9137-9142.

4. V. K. Zaitsev, M. I. Fedorov, E. A. Gurieva, I. S. Eremin, P. P. Konstantinov, A. Y. Samunin and M. V. Vedernikov, *Phys. Rev. B*, 2006, **74**, 045207.
5. W. Liu, X. J. Tan, K. Yin, H. J. Liu, X. F. Tang, J. Shi, Q. J. Zhang and C. Uher, *Phys. Rev. Lett.*, 2012, **108**.
6. X. H. Liu, T. J. Zhu, H. Wang, L. P. Hu, H. H. Xie, G. Y. Jiang, G. J. Snyder and X. B. Zhao, *Adv. Energy Mater.*, 2013, **3**, 1238-1244.
7. W. Liu, X. Tang and J. Sharp, *J. Phys. D: Appl. Phys.*, 2010, **43**, 085406.
8. A. U. Khan, N. V. Vlachos, E. Hatzikraniotis, G. S. Polymeris, C. B. Lioutas, E. C. Stefanaki, K. M. Paraskevopoulos, I. Giapintzakis and T. Kyratsi, *Acta Mater.*, 2014, **77**, 43-53.
9. P. Gao, I. Berkun, R. Schmidt, M. Luzenski, X. Lu, P. Bordon Sarac, E. Case and T. Hogan, *J. Electron. Mater.*, 2013, DOI: 10.1007/s11664-013-2865-8, 1-14.
10. T. Dasgupta, C. Stiewe, J. de Boor and E. Müller, *physica status solidi (a)*, 2014, DOI: 10.1002/pssa.201300196, 1250–1254.
11. J.-i. Tani and H. Kido, *J. Alloys Compd.*, 2008, **466**, 335-340.
12. A. Y. Samunin, V. K. Zaitsev, P. P. Konstantinov, M. I. Fedorov, G. N. Isachenko, A. T. Burkov, S. V. Novikov and E. A. Gurieva, *J. Electron. Mater.*, 2013, **42**, 1676-1679.
13. T. Sakamoto, T. Iida, Y. Honda, M. Tada, T. Sekiguchi, K. Nishio, Y. Kogo and Y. Takanashi, *J. Electron. Mater.*, 2012, **41**, 1805-1810.
14. J. de Boor, C. Gloanec, H. Kolb, R. Sottong, P. Ziolkowski and E. Müller, *J. Alloys Compd.*, 2015, **632**, 348-353.
15. J. Bourgeois, J. Tobola, B. Wiendlocha, L. Chaput, P. Zwolenski, D. Berthebaud, Q. Recour, F. Gascoin and H. Scherrer, *Functional Materials Letters*, 2013, **06**, 1340005.
16. S. F. Muntyanu, E. B. Sokolov and E. S. Makarov, *Zh. Neorgan. Mater.*, 1966, **2**, 870-875.
17. A. Kozlov, J. Grobner and R. Schmid-Fetzer, *J. Alloys Compd.*, 2011, **509**, 3326-3337.
18. L. D. Zhao, V. P. Dravid and M. G. Kanatzidis, *Energ Environ Sci*, 2014, **7**, 251-268.
19. W. J. Xie, J. He, S. Zhu, X. L. Su, S. Y. Wang, T. Holgate, J. W. Graff, V. Ponnambalam, S. J. Poon, X. F. Tang, Q. J. Zhang and T. M. Tritt, *Acta Mater.*, 2010, **58**, 4705-4713.
20. J. H. Bahk, Z. X. Bian and A. Shakouri, *Phys. Rev. B*, 2014, **89**.
21. W. Liu, H. Chi, H. Sun, Q. Zhang, K. Yin, X. Tang, Q. Zhang and C. Uher, *PCCP*, 2014, **16**, 6893-6897.
22. T. Dasgupta, C. Stiewe, R. Hassdorf, A. J. Zhou, L. Boettcher and E. Mueller, *Phys. Rev. B*, 2011, **83**.
23. J. de Boor, C. Compere, T. Dasgupta, C. Stiewe, H. Kolb, A. Schmitz and E. Mueller, *J Mater Sci*, 2014, **49**, 3196-3204.
24. J. de Boor, C. Stiewe, P. Ziolkowski, T. Dasgupta, G. Karpinski, E. Lenz, F. Edler and E. Mueller, *J. Electron. Mater.*, 2013, **42**, 1711-1718.
25. J. de Boor and E. Muller, *Rev. Sci. Instrum.*, 2013, **84**, 065102.
26. L. J. van der Pauw, *Philips Res. Rep.*, 1958, **13**, 1-9.
27. K. A. Borup, J. de Boor, H. Wang, F. Drymiotis, F. Gascoin, X. Shi, L. Chen, M. I. Fedorov, E. Muller, B. B. Iversen and G. J. Snyder, *Energ Environ Sci*, 2015, **8**, 423-435.
28. J. de Boor, T. Dasgupta, H. Kolb, C. Compere, K. Kelm and E. Mueller, *Acta Mater.*, 2014, **77**, 68-75.
29. A. F. May and G. J. Snyder, in *Thermoelectrics and its Energy Harvesting*, ed. D. M. Rowe, CRC Press, 2012, ch. 11.
30. S. K. Bux, M. T. Yeung, E. S. Toberer, G. J. Snyder, R. B. Kaner and J. P. Fleurial, *J. Mater. Chem.*, 2011, **21**, 12259-12266.
31. A. F. May, E. S. Toberer, A. Saramat and G. J. Snyder, *Phys. Rev. B*, 2009, **80**.
32. Y. L. Tang, Y. T. Qiu, L. L. Xi, X. Shi, W. Q. Zhang, L. D. Chen, S. M. Tseng, S. W. Chen and G. J. Snyder, *Energ Environ Sci*, 2014, **7**, 812-819.
33. M. I. Fedorov and V. K. Zaitsev, in *CRC Handbook of thermoelectrics: Macro to Nano*, ed. D. M. Rowe, CRC, Boca Raton, USA, 2006, p. 31.
34. S. Fiameni, S. Battiston, S. Boldrini, A. Famengo, F. Agresti, S. Barison and M. Fabrizio, *J. Solid State Chem.*, 2012, **193**, 142-146.
35. X. J. Tan, W. Liu, H. J. Liu, J. Shi, X. F. Tang and C. Uher, *Phys. Rev. B*, 2012, **85**.
36. D. A. Pshenai-Severin, M. I. Fedorov and A. Y. Samunin, *J. Electron. Mater.*, 2013, **42**, 1707-1710.
37. W. Zawadzki, *Advances in Physics*, 1974, **23**, 435-522.
38. W. B. Whitten, P. L. Chung and G. C. Danielson, *J. Phys. Chem. Solids*, 1965, **26**, 49-56.
39. L. C. Davis, W. B. Whitten and G. C. Danielson, *J. Phys. Chem. Solids*, 1967, **28**, 439-447.
40. B. Klobes, personal communication.
41. Y. Hayatsu, T. Iida, T. Sakamoto, S. Kurosaki, K. Nishio, Y. Kogo and Y. Takanashi, *J. Solid State Chem.*, 2012, **193**, 161-165.
42. H. Wang, A. D. LaLonde, Y. Z. Pei and G. J. Snyder, *Adv. Funct. Mater.*, 2013, **23**, 1586-1596.

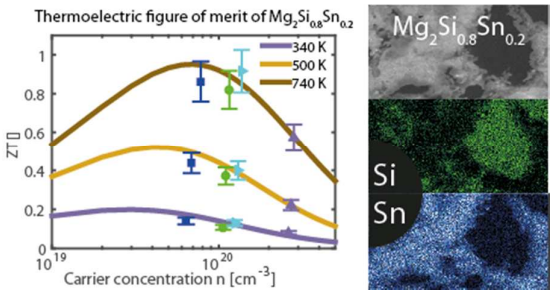

We have optimized the thermoelectric material $Mg_2Si_{0.8}Sn_{0.2}$ and analyze the electronic transport employing a single parabolic band model.